Chemical Engineering Journal 516 (2025) 164129

Contents lists available at ScienceDirect

Chemical Engineering Journal

journal homepage: www.elsevier.com/locate/cej

Boosted thermal redox desalination of seawater driven by gradient of redox electrolyte

Wenning Gao [a], Dian Zhang [a,b], Lu Guo [c], Danling Tang [d], Guangguo Ying [e], Fuming Chen [a,b,c,e,*]

[a] *Guangdong Provincial Key Laboratory of Quantum Engineering and Quantum Materials, School of Electronic Science and Engineering (School of Microelectronics), South China Normal University, 528225, China*
[b] *Collaborative Innovation Center of Ecological Civilization, School of Chemistry and Chemical Engineering, Hainan University, Haikou 570228 China*
[c] *Yunnan Key Laboratory of Electromagnetic Materials and Devices, School of Engineering, Yunnan University, Kunming 650091, China*
[d] *Southern Marine Science and Engineering Guangdong Laboratory (Guangzhou), Guangzhou 511458, China*
[e] *Environmental Research Institute/School of Environment, Guangdong Provincial Key Laboratory of Chemical Pollution and Environmental Safety & MOE Key Laboratory of Theoretical Chemistry of Environment, South China Normal University, Guangzhou, Guangdong 510006, China*

ARTICLE INFO

Keywords:
Thermal redox desalination
Coupled thermocell
Redox electrolyte gradient
Salt removal performance
Scalability

ABSTRACT

Electrolyte-based thermal redox desalination (ETRD) offers an alternative approach to freshwater production in regions with limited electricity. However, maintaining the redox electrolyte gradient between the two electrodes has limited its practical application. To address this challenge, we introduce a reactivation ETRD system that employs $Fe(CN)_6^{4-}/Fe(CN)_6^{3-}$ electrolytes flowing separately through hot and cold chambers. Electrolyte gradient is sustained through an external reactivation loop utilizing $LiFePO_4$ and Prussian blue (PB). With the maintained gradient of redox electrolyte, the coupled thermocell achieves a remarkable Seebeck coefficient (S_e) of 1.88 mV K^{-1}, an open-circuit voltage of 311 mV at a temperature difference (ΔT) of 50 K—1.67 times higher than the highest reported value for thermoelectric systems using aqueous $Fe(CN)_6^{4-}/Fe(CN)_6^{3-}$, and a temperature-insensitive maximum power density of 0.635 mW m^{-2} K^{-2}. Accordingly, the ETRD device, operating under the maintained electrolyte gradient, exhibits competitive salt removal performance, and can produce freshwater while simultaneously generating electricity, rather than consuming it. Scalability was demonstrated by connecting 10 units in series. This work presents a novel approach to designing high-performance ETRD for efficient low-grade heat harvesting and seawater desalination.

1. Introduction

The growing global freshwater shortage, driven by increasing water consumption and climate change, necessitates the development of new freshwater production technologies [1–3]. Given the vast reserves of seawater, various desalination techniques have emerged as a potential solution for ensuring an adequate freshwater supply [4–6]. However, conventional seawater desalination methods face significant challenges. Reverse osmosis (RO), for instance, consumes substantial amounts of electrical energy and is susceptible to membrane contamination and fouling [7–9]. While capacitive deionization (CDI) and redox flow desalination (RFD) require less energy than RO, their need for a continuous power supply still limits their widespread application, particularly in regions or situations with limited electricity access [10–14]. Solar-driven photoelectrochemical desalination (SD-PED), while promising, is hindered by the intermittent nature of solar energy and poor long-term stability due to rapidly declining photocurrent [15–17]. Consequently, the development of novel seawater desalination technologies that utilize alternative or sustainable energy sources is crucial, especially for areas lacking reliable electricity or solar energy [18–21].

Thermocells have garnered significant research interest in recent decades due to their potential to harness readily available low-grade heat from sources such as power plants, vehicle engines, data centers, microelectronics, human bodies, and geothermal energy, to provide the necessary temperature difference for operation [22,23]. Furthermore,

---

* Corresponding author at: Guangdong Provincial Key Laboratory of Quantum Engineering and Quantum Materials, School of Electronic Science and Engineering (School of Microelectronics), South China Normal University, 528225, China.

E-mail address: chenfumsg@gmail.com (F. Chen).

https://doi.org/10.1016/j.cej.2025.164129
Received 15 March 2025; Received in revised form 22 May 2025; Accepted 24 May 2025

the $Fe(CN)_6^{4-}/Fe(CN)_6^{3-}$ redox couple is frequently employed in aqueous thermocells due to its favorable combination of low cost, environmental compatibility, good redox stability, and particularly its high reaction entropy change, leading to a large Seebeck coefficient [24]. Inspired by this, our group recently reported an ETRD device that integrates a salinized chamber and a desalinized chamber with a conventional redox-induced thermocell containing $Fe(CN)_6^{4-}/Fe(CN)_6^{3-}$ electrolytes [25]. Applying a temperature difference across the device drives desalination of the salt stream within the desalinized chamber. Critically, this technology holds promise for utilizing abundant low-grade waste heat (<100℃) rather than electricity or solar energy, to power seawater desalination. Besides, this approach supplies power to external during desalination, unlike CDI and RFD, which consume electricity. Despite these advantages, the desalination performance of the ETRD device is currently constrained by the difficulty in maintaining the redox electrolyte gradient between the two electrodes.

The performance of an ETRD device is dependent on the thermoelectric performance of the coupled thermocell. Typically, conventional aqueous thermocells exhibit limited thermoelectric conversion capability, characterized by a low Seebeck coefficient (S_e) and modest output power density [26–28]. Consequently, the previously reported ETRD device displays a limited desalination performance [25]. Therefore, enhancing the S_e and output power density of the thermocell can directly improve the coupled ETRD's performance. As detailed in the mechanistic analysis (Supplementary Text 1), increasing the redox electrolyte gradient ($Grad_{RE}$) can effectively enhance the S_e of a thermocell. Previous studies have demonstrated that introducing additives for thermosensitive crystallization can increase $Grad_{RE}$, thereby boosting S_e [29–32]. Furthermore, a high $Grad_{RE}$ in thermocell facilitates charge exchange between the electrode and the electrolyte, leading to a higher output current and, consequently, enhanced power density [28]. Thus, an ETRD device coupled with a thermocell optimized for a high $Grad_{RE}$ will exhibit significantly improved desalination capabilities.

Building upon these considerations and combined with numerous research advancements in novel electrochemical systems, including modeling and transport studies [33–36], we propose a novel two-chamber liquid thermocell, separated into hot and cold chambers by a cation exchange membrane (CEM). Pure $Fe(CN)_6^{4-}/Fe(CN)_6^{3-}$ electrolytes flow independently through the hot and cold chambers, respectively. During discharge, $LiFePO_4$ and Prussian blue (PB) act as reactivators within an external loop, maintaining the purity of the $Fe(CN)_6^{4-}$ and $Fe(CN)_6^{3-}$ electrolytes in the hot and cold chambers, respectively. This design allows the thermocell to operate continuously at a high $Grad_{RE}$, resulting in an enhanced Seebeck coefficient (S_e) and significantly improved power density. Consequently, the optimized ETRD device exhibits competitive salt removal performance. Notably, in contrast to conventional electricity-consuming desalination techniques, the ETRD system generates external power during the desalination process. This work offers valuable insights into the design of high-performance ETRD systems for efficient low-grade heat harvesting and seawater desalination.

2. Material and methods

2.1. Chemicals and materials

Lithium iron phosphate ($LiFePO_4$) was purchased from Shenzhen BTR New Energy Materials Co. Ltd, China. Prussian blue (PB) was purchased from Macklin. Sodium ferrocyanide ($Na_4Fe(CN)_6$), sodium ferricyanide ($Na_3Fe(CN)_6$), and other chemicals were purchased from Shanghai Aladdin Ltd, China. All chemicals were of analytical purity and used without further treatment. The ion exchange membranes (AEM/CEM, standard grade) were purchased from Tokuyama, Japan. Graphite papers were purchased from Beijing Jinlong Special Carbon Co. Ltd. China.

2.2. Preparation of $LiFePO_4$ and PB electrodes, $LiFePO_4$ and PB granules

$LiFePO_4$ electrode and $LiFePO_4$ granules were prepared as follows. First, pristine $LiFePO_4$, carbon black, and polyvinylidene difluoride (weight ratio: 8: 1: 1) were stirred into a slurry with NMP as solvent. Then, part of the slurry was uniformly coated on a graphite paper (1 × 1 cm^2). After drying the treated graphite paper in vacuum for 12 h at 60 ℃, $LiFePO_4$ electrode was acquired. The remaining part of the slurry was evenly coated on a petri dish and vacuum-dried for 12 h at 60 ℃. Thereafter, the dry coating was broken into $LiFePO_4$ granules (**Fig. S2**).

PB electrode and PB granules (**Fig. S2**) were prepared with the same method as preparing $LiFePO_4$ electrode and $LiFePO_4$ granules, except that pristine $LiFePO_4$ was replaced with pristine PB.

2.3. Measurements and material characterizations

The open-circuit voltage, current–voltage curve, short-circuit current and cyclic voltammetry (CV) were implemented on a CHI 660E electrochemical workstation. The open-circuit voltage, current–voltage curve, and short-circuit current were directly measured on the coupled thermocell. CV curve of the $Fe(CN)_6^{4-/3-}$ couple was tested in a typical three-electrode system containing 50 mM/50 mM $Fe(CN)_6^{4-/3-}$ at a scan rate of 5 mV s^{-1}, with an Ag/AgCl electrode as the reference electrode, and two Pt sheets as the working and counter electrodes, respectively. CV curve of the $LiFePO_4$ or PB electrode was tested in a typical three-electrode system containing 0.5 M LiCl at a scan rate of 0.5 mV s^{-1}, with the $LiFePO_4$ or PB electrode as the working electrode, an Ag/AgCl electrode as the reference electrode, and a Pt sheet as the counter electrode, respectively.

The temperature difference was monitored by a thermocouple data logger (620L). The real-time conductivity was recorded with a conductivity meter (eDAQ, EPU357). The ion concentrations were detected by inductively coupled plasma optical emission spectrometer (ICP-OES). X-ray diffraction (XRD) data were tested from an X-ray diffractometer (Bruker D8 Advance) with Cu/Ka radiation, $\lambda = 0.15406$ nm, 40 kV, 40 mA. Ultraviolet–visible (UV–Vis) spectroscopy was tested using a UV–Vis spectrophotometry (Shimadzu UV-2600). Scanning electron microscope (SEM, FEI QUANTA 2000) weas employed to analyze the microstructure and morphology. Fourier transform infrared spectrometer (FTIR, Nicolet 6700) was used to collect the FTIR spectra.

2.4. Calculation of performance parameters

Power density (P, W m^{-2}).

The power output per unit area of the thermocell was calculated with eq. (1):

$$P = \frac{U \times I}{A} \tag{1}$$

Where, U (V) and I (A) are the voltage and corresponding current of the current–voltage curve, respectively, and A (m^2) is the effective area of the device. Additionally, $P_{\max}$ is the maximum value of the power density.

Effective electrical conductivity (σ_{eff}, S m^{-1}).

The effective electrical conductivity of the thermocell was calculated from the slope of the current–voltage curve. The specific formula can be expressed as eq. (2):

$$\sigma_{eff} = \frac{\Delta d \times G}{A} \tag{2}$$

Where, Δd (m) is the distance between the hot and cold electrodes of the device, A (m^2) is the effective area of the device, and G (S) is the slope of the current–voltage curve.

Effective thermal conductivity (κ_{eff}, W m^{-1} K^{-1}).

Because of the complex internal structure of the thermocell, we used a relatively simple steady-state method to evaluate effective thermal conductivity. The steady-state method is based on the heat flux conservation law, which ignores the heat loss in the vertical direction of heat transport. Here we assume that the heat transported through the graphite electrode on the hot side, the graphite electrode on the cold side, and the interior of the device is Q_1, Q_2, and Q, respectively. Therefore, the heat transport of the liquid thermocell (LTC) device can be simplified as eq. (3):

$$Q_1 = Q_2 = Q \tag{3}$$

Based on the above discussion, the thermal transport in the LTC can be simplified as **Fig. S20**. According to the thermal transport formula eq. (4), eq. (3) can be expressed as eq. (5):

$$Q = \kappa A \frac{\Delta T}{\Delta d} \tag{4}$$

$$\kappa A \frac{\Delta T_1}{d} = \kappa A \frac{\Delta T_2}{d} = \kappa_{eff} A \frac{\Delta T}{\Delta d} \tag{5}$$

Where κ (W m^{-1} K^{-1}) is the thermal conductivity of the graphite paper, A (m^2) is the effective area of the device, d (mm) is the thickness of the graphite paper, and Δd (mm) is the distance between the two graphite electrodes. Then, effective thermal conductivity can be calculated.

Figure of merit (ZT).

The figure of merit (ZT) is an important parameter to characterize the performance of a thermoelectric device, which can be expressed as eq. (6):

$$ZT = \frac{S_e^2 \times \sigma_{eff} \times \overline{T}}{\kappa_{eff}} \tag{6}$$

$$\overline{T} = \frac{T_H + T_C}{2} \tag{7}$$

S_e(V K^{-1}) is the Seebeck coefficient of the device. T_H (K) and T_C (K) are the temperatures of the hot and cold electrodes, respectively. σ_{eff} (S m^{-1}) and κ_{eff} (W m^{-1} K^{-1}) are the effective electrical conductivity and effective thermal conductivity, respectively.

Carnot-relative efficiency (η_r, %)

Carnot-relative efficiency (η_r) is generally used to evaluate the energy-conversion performance, which is expressed as eq. (8):

$$\eta_r = \frac{\eta_1}{\eta_c} \tag{8}$$

$$\eta_1 = \frac{T_H - T_C}{T_H} \times \frac{\sqrt{1+ZT} - 1}{\sqrt{1+ZT} - T_C/T_H} \tag{9}$$

$$\eta_c = \frac{\Delta T}{T_H} \tag{10}$$

Where, η_1 is the thermoelectric conversion efficiency, η_c is the Carnot efficiency, ZT is the figure of merit, T_H (K) and T_C (K) are the temperatures of the hot and cold electrodes, respectively.

Heat input power density (P_{heat}, KWm^{-2})

The heat input power density is the heat flux through the device, which can be expressed as eq. (S11):

$$P_{heat} = \kappa_{eff} \frac{\Delta T}{\Delta d} \tag{11}$$

Where κ_{eff} is the Effective thermal conductivity, ΔT is the temperature difference, and Δd is the distance between the hot and cold electrodes.

Temperature-insensitive maximum power density ($P_{max}/(\Delta T)^2$, mW m^{-2} K^{-2}).

The temperature-insensitive maximum power density ($P_{max}/(\Delta T)^2$) is also an important performance parameter to evaluate the performance of thermocells, which can be expressed as:

$$P_{max}/(\Delta T)^2 = \frac{U \times I}{4 \times A \times \Delta T^2} \tag{12}$$

Where U (V) and I (mA) are the voltage and corresponding current of the current–voltage curve, respectively, A (m^2) is the effective area of the device, and ΔT (K) is the temperature difference between two electrodes.

Salt removal rate ($\overline{v}$, μg cm^{-2} min^{-1}).

The salt removal rate reflects the average amount of salt removed per unit area and unit time of the ETRD device during the seawater desalination, which can be expressed as:

$$\overline{v} = \frac{(C_0 - C_t) \times V}{A \times t} \tag{13}$$

Where C_0 (ppm) and C_t (ppm) are the initial concentration and final concentration of the seawater, respectively, V (L) is the volume of the seawater, A (cm^2) is the effective area of the device during the seawater desalination, t (min) is the total time taken for the desalination of seawater to freshwater.

Energy efficiency for desalination ($\eta_{desalination}$, %)

The energy efficiency for desalination reflects the thermoelectric conversion efficiency of the device during the desalination process, which can be expressed as:

$$\eta_{desalination} = \frac{\int_0^t i^2 R dt}{P_{heat} \times t} \tag{14}$$

Where i (A), t (s), R (Ω), and P_{heat} (W) represent the desalination current, the desalination time, the resistance of the device, and the heat power input, respectively.

3. Results and discussion

3.1. *Principle and realization of thermocell operating at a highGrad$_{RE}$*

The schematic diagram of the thermocell is illustrated in Fig. 1**a**. Two graphite paper electrodes serve as the working electrodes, while a cation exchange membrane (CEM) separates the device into hot and cold chambers. Pure $Fe(CN)_6^{4-}$ and $Fe(CN)_6^{3-}$ electrolytes flow independently through the hot and cold chambers, respectively. Upon applying a temperature difference (ΔT), thermosensitive $Fe(CN)_6^{4-}$ ions in the hot chamber are oxidized to $Fe(CN)_6^{3-}$ ions, releasing electrons to the external circuit. Simultaneously, $Fe(CN)_6^{3-}$ ions in the cold chamber accept these electrons and are reduced to $Fe(CN)_6^{4-}$ ions. Over time, the initially high *Grad$_{RE}$* of the thermocell decreases. The detailed experimental setup is illustrated in **Fig. S1**.

To maintain the high *Grad$_{RE}$* of the thermocell, selecting appropriate reactivators in external loops is crucial. Our exploration shows that $LiFePO_4$ can effectively reduce $Fe(CN)_6^{3-}$ ion, as evidenced by its lower redox potential compared to the $Fe(CN)_6^{4-/3-}$ couple (Fig. 1**b**). This is further confirmed by the faded color of the $Fe(CN)_6^{3-}$ solution after contact with $LiFePO_4$ granules (Fig. 1**c**), the lighter appearance of $LiFePO_4$ granules after reaction (**Fig. S2**), and the new peaks corresponding to $FePO_4$ (PDF 96 –152-5577) observed in the XRD pattern of the reacted $LiFePO_4$ (Fig. 1**d**). These observations indicate that $LiFePO_4$ is capable of reducing the $Fe(CN)_6^{3-}$ electrolyte [37]. The reaction can be expressed as:

$$Fe(CN)_6^{3-} + LiFePO_4 \rightarrow Fe(CN)_6^{4-} + FePO_4 + Li^+ \tag{15}$$

$FePO_4$ from the reaction can be directly recycled into $LiFePO_4$, a standard procedure for lithium-ion batteries, enabling the reuse of the material in this work [38,39].

Similarly, the higher redox potential of PB compared to $Fe(CN)_6^{4-/3-}$ couple (Fig. 1**b**), the darkened $Fe(CN)_6^{4-}$ solution in the presence of PB

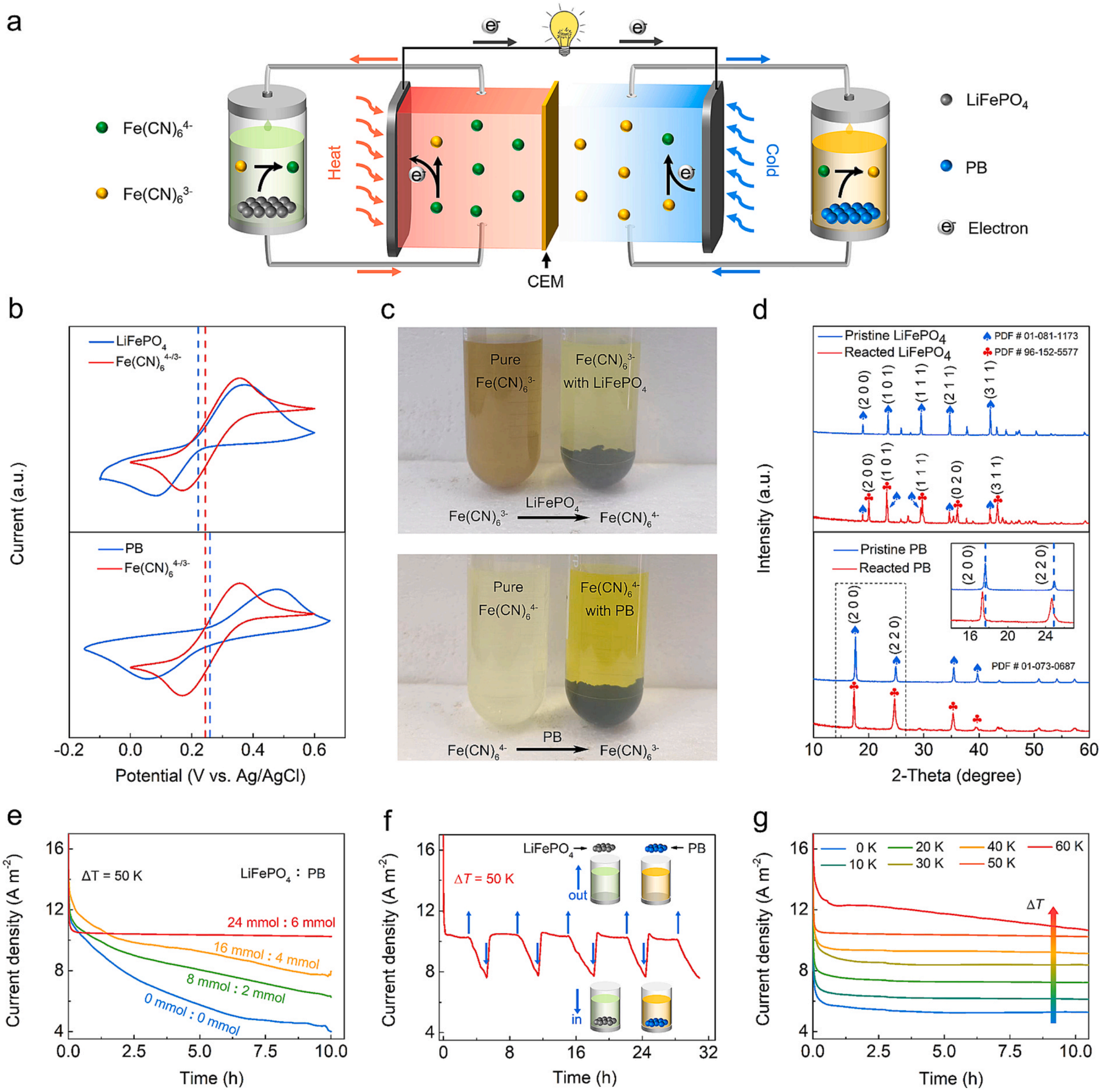

Fig. 1. (a) Schematic diagram of the coupled thermocell in this work. (b) CV curves of $Fe(CN)_6^{4-/3-}$, $LiFePO_4$, and PB. (c) Comparison between pure $Fe(CN)_6^{3-}$ solution and $Fe(CN)_6^{3-}$ solution with $LiFePO_4$ granules (Reaction time: 48 h), between pure $Fe(CN)_6^{4-}$ solution and $Fe(CN)_6^{4-}$ solution with PB granules (Reaction time: 48 h). (d) XRD patterns of pristine $LiFePO_4$, $LiFePO_4$ reacted with pure $Fe(CN)_6^{3-}$ solution, pristine PB, and PB reacted with pure $Fe(CN)_6^{4-}$ solution. (e) Short-circuit currents of the thermocell with different quantities of $LiFePO_4$ and PB granules (0:0, 8 mmol: 2 mmol, 16 mmol: 4 mmol, 24 mmol: 6 mmol). (f) Short-circuit current of the thermocell with both $LiFePO_4$ and PB granules repeatedly inserted and removed. (g) Short-circuit currents of the thermocell operating at different ΔT.

granules (Fig. 1c), the darker appearance of PB granules after the reaction (**Fig. S2**), and the negatively shifted characteristic peaks corresponding to (200) and (220) crystal planes of PB after the reaction (Fig. 1**d**) indicate that PB facilitates the oxidation of the $Fe(CN)_6^{4-}$ ion [5,40]. The reaction can be expressed as:

$$4Na^{+} + 4Fe(CN)_6^{4-} + Fe_4\left[Fe(CN)_6\right]_3 \rightarrow 4Fe(CN)_6^{3-} + Na_4Fe_4\left[Fe(CN)_6\right]_3 \tag{16}$$

The results are consistent with redox flow energy storage [40–42]. The generated $Na_4Fe_4[Fe(CN)_6]_3$ can be restored to $Fe_4[Fe(CN)_6]_3$ through a simple charging process, allowing its reuse as a cathode material and promoting the cyclic use of the material in this work [43]. Therefore, $LiFePO_4$ and PB are selected as the reactivators to maintain the high $Grad_{RE}$ of the thermocell.

$LiFePO_4$ and PB are further confirmed to effectively maintain the high $Grad_{RE}$ of the thermocell. We first examined the optimal quantities of $LiFePO_4$ and PB granules required. The relevant device parameters are listed in **Table S1**. Fig. 1**e** shows the short-circuit currents of the thermocell at 50 K temperature gradient, with varying masses of $LiFePO_4$ and PB granules in **Table S2**. With the quantity rise of the granules, the short-circuit current tends to stabilize due to the large contact area between the granules and electrolytes, which accelerates the reduction of $Fe(CN)_6^{3-}$ in $Fe(CN)_6^{4-}$ electrolyte and the oxidation of $Fe(CN)_6^{4-}$ in $Fe(CN)_6^{3-}$ electrolyte. With 24 mmol of $LiFePO_4$ granules and 6 mmol of PB granules, the thermocell achieved a relatively stable short-circuit current for 10 h. Therefore, these quantities are identified as the optimal quantities. Ultraviolet–visible (UV–Vis) spectroscopy was further employed to measure the concentration ratios of $Fe(CN)_6^{3-}$ to $Fe(CN)_6^{4-}$ (**Figs. S3**). Both pristine and reacted $Fe(CN)_6^{4-}$ electrolyte with $LiFePO_4$ as reactivator display the characteristic absorption peak of $Fe(CN)_6^{4-}$ at 217 nm (**Fig. S3c**)[44]. The intensity ratio of the peaks

(~0.97) demonstrates that $LiFePO_4$ maintains the purity of $Fe(CN)_6^{4-}$ electrolyte. Similarly, In **Fig. S3d**, both pristine and reacted $Fe(CN)_6^{3-}$ electrolyte with PB as reactivator exhibit the characteristic absorption peaks of $Fe(CN)_6^{3-}$ at 260, 303, 320, and 420 nm[32,44]. The nearly identical intensity of the absorption peaks confirms that PB preserves the purity of $Fe(CN)_6^{3-}$ electrolyte. The above facts indicate that $LiFePO_4$ and PB maintain the high $Grad_{RE}$ of the thermocell. Fig. 1**f** shows the short-circuit current of the optimized thermocell in the reactivation cycling test at ΔT of 50 K, with $LiFePO_4$ and PB granules repeatedly inserted and removed, further validating their roles in maintaining the high $Grad_{RE}$ of the thermocell. The long-term stability and degradation rates of the reactivation materials in the reactivation cycling test were analyzed in Supplementary Text 3.

Moreover, the optimized thermocell also exhibits stable short-circuit currents at ΔT values ranging from 0 to 40 K (Fig. 1**g**). The increased short-circuit current reflects the fast thermoelectric reaction at high temperature gradient. The reduced current at 60 K may result from side reactions at elevated temperatures, such as degradation of both the redox electrolyte and the ion exchange membrane. Hence, $LiFePO_4$ and PB maintain the high $Grad_{RE}$ of the thermocell.

3.2. Thermoelectric performance of the coupled thermocell operating at a high$Grad_{RE}$

For further clarity, we will denote the electrolyte concentration in the thermocell as:

$$\left[Fe(CN)_6^{4-}\right]_{hot} : \left[Fe(CN)_6^{3-}\right]_{hot} \| \left[Fe(CN)_6^{4-}\right]_{cold} : \left[Fe(CN)_6^{3-}\right]_{cold} \tag{17}$$

The subscripts 'hot' and 'cold' refer to the corresponding hot and cold chambers, respectively. The unit of concentration is mol L^{-1}. When pure $Fe(CN)_6^{4-}$ and $Fe(CN)_6^{3-}$ electrolytes flow separately in the hot and cold chambers, the expression can be represented below:

$$\left[Fe(CN)_6^{4-}\right]_{hot} : 0 \| 0 : \left[Fe(CN)_6^{3-}\right]_{cold} \tag{18}$$

Due to the high $Grad_{RE}$ resulted from the nearly pure $Fe(CN)_6^{4-}$ and $Fe(CN)_6^{3-}$ electrolytes (0.2:0||0:0.2) separately in the hot and cold chambers, a high S_e of 1.88 mV K^{-1} can be achieved (Fig. 2**a**). The open-circuit voltage rises from 217 mV at 0 K ΔT to 311 mV at 50 K ΔT. The non-zero open-circuit voltage at 0 K of ΔT is because the different concentration ratios of $Fe(CN)_6^{3-}$ to $Fe(CN)_6^{4-}$ nearby electrodes, as explained in Supplementary Text 2. The maximum power density

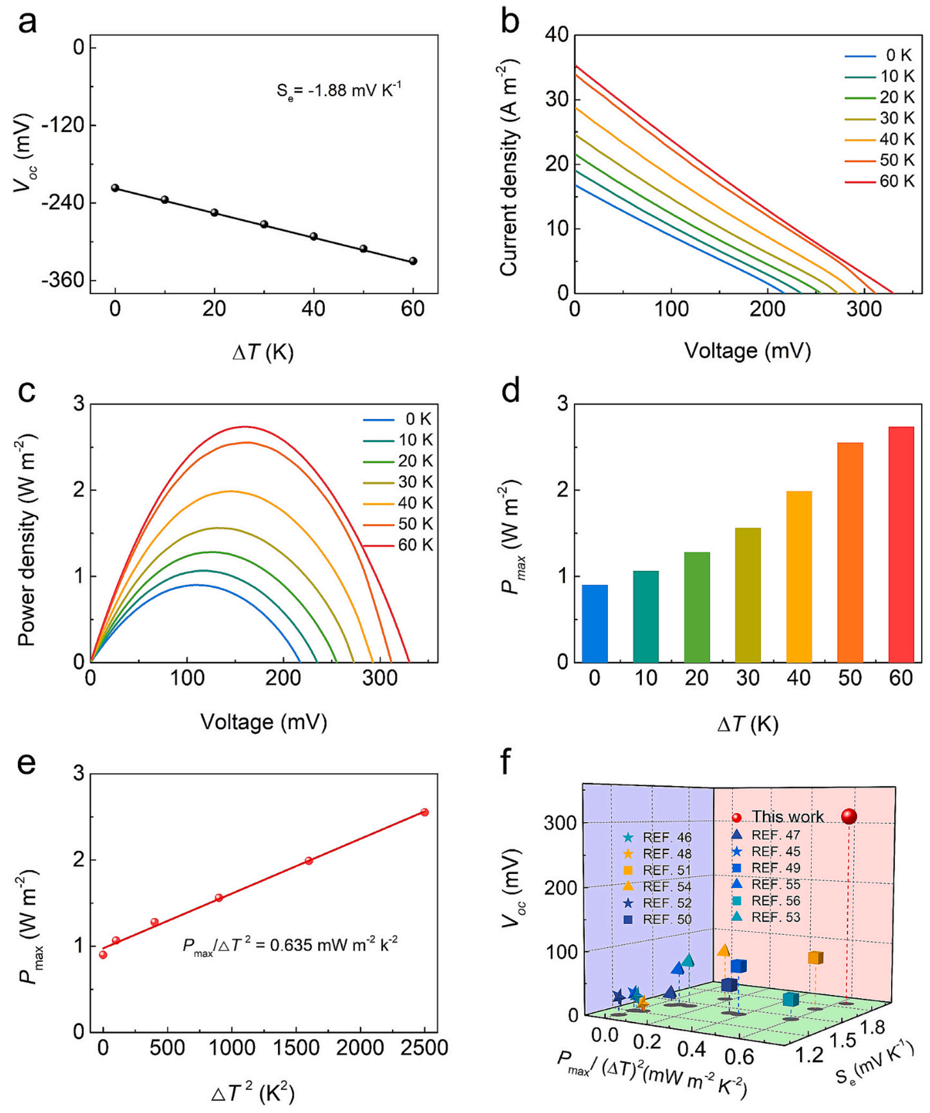

Fig. 2. (a) Open-circuit voltages, (b) Current density–voltage curves, (c) Power density–voltage curves, (d) Maximum power densities, (e) Temperature-insensitive maximum power density ($P_{max}/(\Delta T)^2$) of the thermocell at the electrolyte concentration of 0.2:0||0:0.2. (f) Comparison of the S_e, open-circuit voltage, and $P_{max}/(\Delta T)^2$ with those of previous reported liquid thermocells containing the $Fe(CN)_6^{4-/3-}$ couple.

increases from 0.9 W m^{-2} at 0 K ΔT to 2.55 W m^{-2} at 50 K ΔT in Fig. 2**d**. The temperature-insensitive maximum power density ($P_{max}/(\Delta T)^2$) is 0.635 mW m^{-2} K^{-2} (Fig. 2**e**). **Fig. S4** illustrates the stability of the thermocell's thermoelectric performance, as demonstrated by repeated measurements with error bars. We compare the S_e, open-circuit voltage, and $P_{max}/(\Delta T)^2$ of the thermocell with previously reported liquid thermocells containing the $Fe(CN)_6^{4-/3-}$ couple, highlighting the superior thermoelectric performance of the thermocell in Fig. 2**f** and **Table S3** [45–56]. The heat input power density (P_{heat}) of the thermocell at different ΔT are calculated in **Fig. S5**. Additionally, the effective electrical conductivities, thermal conductivities, ZT values, and Carnot-relative efficiencies of the thermocell at various ΔT are calculated in **Fig. S6**. The reduced effective electrical conductivity at 60 K ΔT leads to low ZT value and Carnot-relative efficiency, resulting in a slow increase in power density when the ΔT rises from 50 K to 60 K. Therefore, the optimal ΔT for the thermocell is determined to be 50 K.

The enhanced thermoelectric performance of the thermocell is attributed to the high $Grad_{RE}$ resulted from nearly pure $Fe(CN)_6^{4-}$/$Fe(CN)_6^{3-}$ electrolytes separately in the hot/cold chambers, as schematically illustrated in Fig. 3**a**. This is further supported by the mechanism analysis in Supplementary Text 1. To verify this, we tested the thermocell at two additional electrolyte concentrations (0.1:0.1||0.1:0.1 and 0.15:0.05||0.05:0.15), and the corresponding thermoelectric performances are displayed in **Figs. S7-S8**. A comparison of the S_e, open-circuit voltage, and maximum power density (Fig. 3**b and 3c**) demonstrates the substantial impact of the high $Grad_{RE}$ on the enhanced thermoelectric performance, thus confirming the validity of our mechanism analysis.

Additionally, scalability was demonstrated by connecting multiple thermocells in series in **Fig. S9-S10**. Ten thermocells in series operating at 0 K ΔT exhibits an open-circuit voltage of approximately 2 V and a maximum power density of around 2 W m^{-2}, and is capable of powering 15 LEDs, as shown in **Fig. S9d and Video S1**. We also conducted the repeated activation experiment confirming the excellent durability of the 10-thermocell system (**Fig. S11**). UV–Vis absorption measurements of the electrolyte (**Fig. S12**) after the repeated activation experiment further verify the effective maintenance of the electrolyte gradient. SEM characterization results (**Fig. S13**) provide compelling evidence for the structural stability of the reactivated materials. The Fourier-transform infrared (FTIR) spectroscopy results (**Fig. S14**) demonstrate that the reactivated materials underwent the transformations described by Equations (15) and (16) during the repeated activation experiment. All these results evidence the practical application potential and durability of multiple thermocells in series.

3.3. Desalination performance of the ETRD device coupled with the optimized thermocell

Fig. 4**a** illustrates the schematic diagram of the ETRD device integrated with the optimized thermocell. This configuration includes two additional chambers—a salinized chamber and a desalinized chamber—positioned between the hot and cold chambers. These chambers are separated by an anion exchange membrane (AEM) and two cation exchange membranes (CEM). The desalinized and salinized streams have identical initial concentrations, volumes, and flow rates, as detailed in **Table S1**.

The desalination mechanism operates as follows: an internal electric field is generated between the electrodes in the hot and cold chambers due to the applied temperature difference and resulting redox reactions. This electric field drives the selective permeation of ions through the ion exchange membranes. Cations from the hot chamber migrate through the CEM towards the cold chamber, while cations from the desalinized chamber migrate through another CEM towards the cold chamber as well. Simultaneously, anions in the desalinized chamber migrate through the AEM towards the salinized chamber. Consequently, this ion movement results in a decreased salt concentration within the desalinized chamber, achieving desalination. Notably, interfacial phenomena including ion selectivity and electrostatic interactions could additionally affect ion transport, suggesting directions for future optimization [57–60].

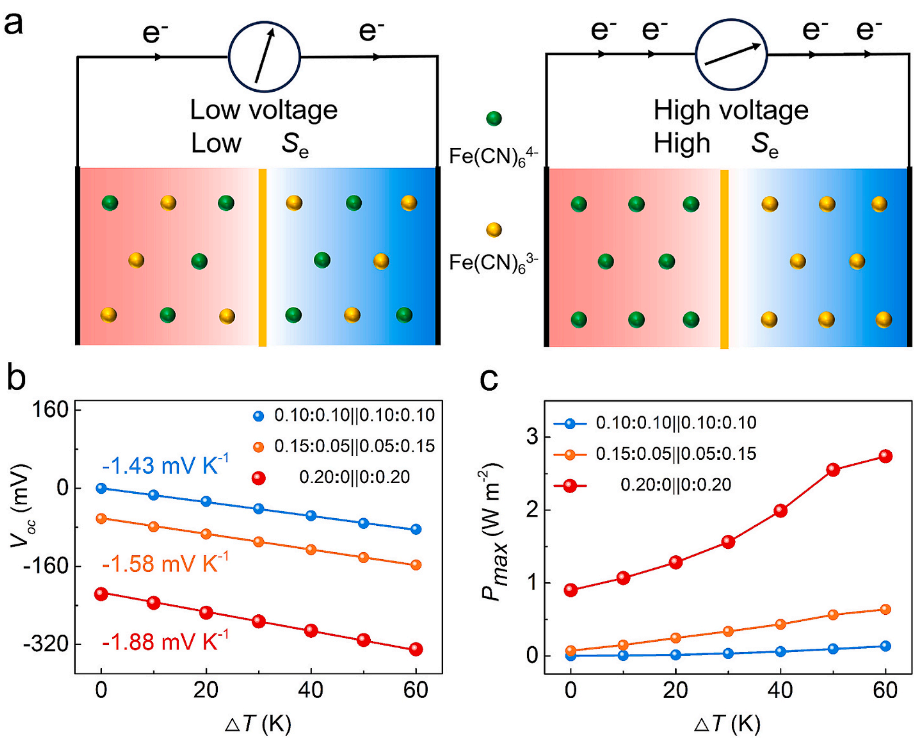

Fig. 3. (a) Mechanism diagram of thermoelectric performance enhancement. (b) Open-circuit voltages and S_e of the thermocell operating at electrolyte concentrations of 0.10:0.10||0.10:0.10, 0.15:0.05||0.05:0.15, and 0.20:0||0:0.20, respectively. (c) Maximum power densities of the thermocell operating at electrolyte concentrations of 0.10:0.10||0.10:0.10, 0.15:0.05||0.05:0.15, and 0.20:0||0:0.20, respectively.

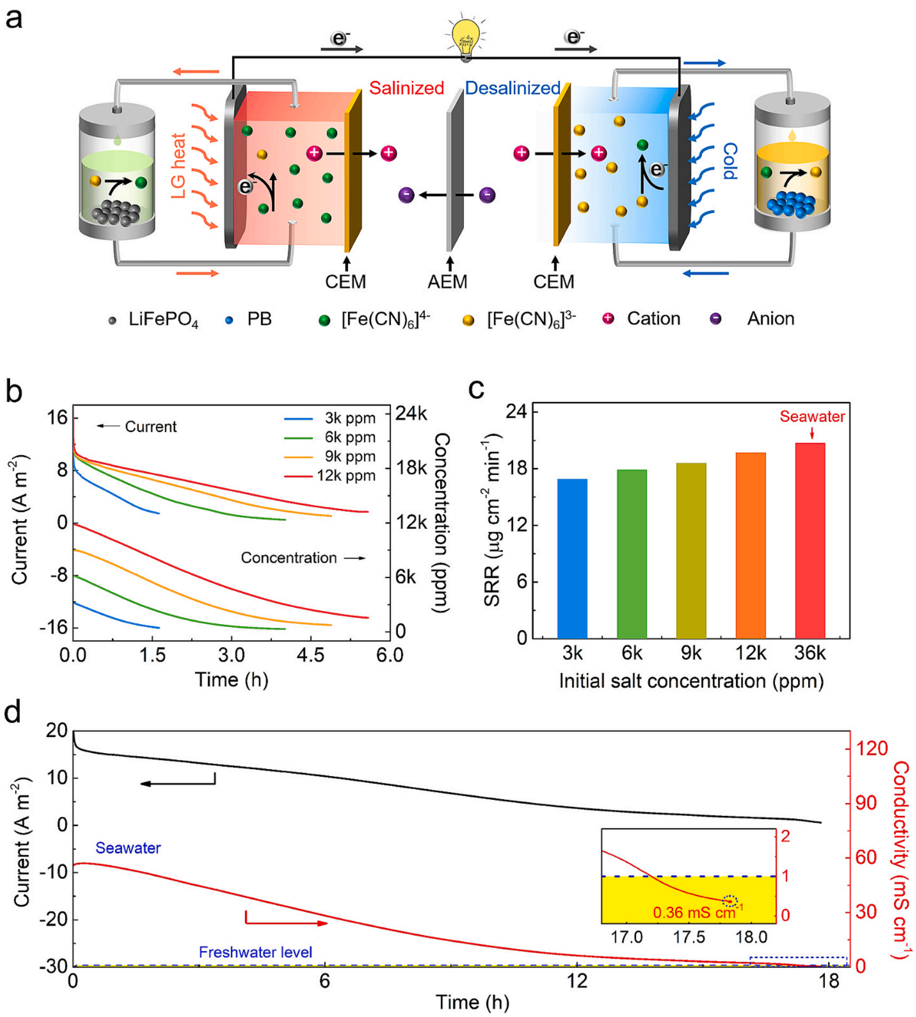

Fig. 4. (a) Schematic diagram of the ETRD device for desalination. (b) Real-time current density and concentration of the desalinized stream with different initial electrolyte concentrations. (c) Salt removal rate (SRR) at different initial salt concentrations. (d) Real-time current density and conductivity of the desalinized stream during seawater desalination.

Desalination tests were conducted using initial salt concentrations of 3000, 6000, 9000, and 12000 ppm. The ETRD device was operated at an optimal ΔT of 50 K, with other parameters as detailed in **Table S1**. Fig. 4**b** displays the real-time current densities and the corresponding concentrations of the desalinized streams. The decreasing concentrations over time confirm successful desalination. The observed reduction in current densities can be attributed to the increased internal impedance resulting from the decreasing salt concentration. As shown in Fig. 4**c**, the salt removal rate (SRR) increased from 16.9 to 19.7 μg cm^{-2} min^{-1} as the initial salt concentration rose from 3000 to 12000 ppm. Cyclic desalination tests using an initial salt concentration of 6000 ppm (**Fig. S15**) confirm stable performance of the device across multiple cycles. To initiate each new cycle, the salt streams within the salinized and desalinized chambers are replenished, while maintaining all other experimental parameters. Additionally, the device's capability for desalination at a reduced temperature gradient (e.g., 20 K, **Fig. S16**), achieving performance comparable to our previous system at higher ΔT [25], further enhances its practical application potential.

Real seawater (collected from Dameisha Park in Shenzhen) desalination was also performed, with an initial conductivity of 56.11 mS cm^{-1}. After 17.2 h of continuous desalination, the seawater's conductivity drops below 1 mS cm^{-1}, meeting freshwater quality standards (Fig. 4**d**). The SRR for real seawater reaches 20.7 μg cm^{-2} min^{-1} in Fig. 4**c**. Notably, the performance of this ETRD device is double that of the only previously reported device, indicating that the high $Grad_{RE}$ of the coupled thermocell significantly enhances desalination performance. Furthermore, the ETRD device demonstrates significantly enhanced energy efficiency for desalination of real seawater (**Fig. S17**).

A comparison between our ETRD device and other desalination techniques is provided in **Table S4**. This comparison demonstrates that ETRD technology offers competitive salt removal performance while simultaneously generating electricity for external use, unlike capacitive deionization (CDI) and redox flow deionization (RFD), which consume electricity. The final conductivity of seawater in our tests reached 0.36 mS cm^{-1}. Inductively coupled plasma-optical emission spectrometry (ICP-OES) measurements before and after desalination, presented in **Table S5**, confirm the exceptional desalination capability of our ETRD device.

4. Conclusion

In summary, we have developed an enhanced electrolyte-based thermal redox desalination (ETRD) device. This device utilizes pure Fe(CN)$_6^{4-}$/Fe(CN)$_6^{3-}$ electrolytes flowing independently through the hot and cold chambers and employs LiFePO$_4$ and Prussian blue as reactivators to maintain electrolyte purity. When applied to seawater desalination, the ETRD device demonstrated competitive salt removal performance while simultaneously generating external power, unlike other electricity-consuming desalination techniques. The high gradient of the redox couple between the two electrodes contributes to the improved Seebeck coefficient (S_e) and output power density, thereby boosting the desalination performance of the ETRD device. Future research will focus on improving the device's figure of merit (ZT) and Carnot-relative efficiency by increasing the effective electrical conductivity and reducing the effective thermal conductivity. We anticipate that ETRD will prove highly effective in low-grade heat harvesting and find broad application in seawater desalination.

CRediT authorship contribution statement

Wenning Gao: Writing – review & editing, Writing – original draft, Validation, Methodology, Investigation, Formal analysis, Data curation, Conceptualization. **Dian Zhang:** Writing – original draft, Validation, Investigation, Formal analysis. **Lu Guo:** Validation, Investigation, Formal analysis. **Danling Tang:** Writing – original draft, Validation, Investigation, Formal analysis. **Guangguo Ying:** Writing – review & editing, Validation, Formal analysis. **Fuming Chen:** Writing – review & editing, Writing – original draft, Validation, Supervision, Project administration, Methodology, Investigation, Funding acquisition, Formal analysis, Conceptualization.

Declaration of competing interest

The authors declare that they have no known competing financial interests or personal relationships that could have appeared to influence the work reported in this paper.

Acknowledgements

This project was funded by National Natural Science Foundation of China (U22A20604, 42030703, 22308304), Yunnan Revitalization Talent Support Program, Guangdong Basic and Applied Basic Research Foundation (2023A1515140065, 2024A1515010924), Key Special Supporting Talent Team Program of Guangdong (2019BT02H594), Key PI Project of Southern Marine Science and Engineering Guangdong Laboratory (Guangzhou) (GML2021GD0810). Additionally, the authors would like to acknowledge the support from the Yunnan Key Laboratory of Carbon Neutrality and Green Low-Carbon Technologies associated with project number 202205AG070002.

Author contributions

W G and F C conceived the project. W G, D Z, and L G carried out material characterization and experimental measurements. W G., D Z., and L G interpreted the partial data. D T. and G Y. interpreted the partial data. All authors participated in discussing the results. W G, L G, D T, G Y and F C prepared and revised the paper with input from all the co-authors.

Appendix A. Supplementary data

Supplementary data to this article can be found online at https://doi.org/10.1016/j.cej.2025.164129.

Data availability

Data will be made available on request.

References

[1] B.R. Scanlon, S. Fakhreddine, A. Rateb, I. de Graaf, J. Famiglietti, T. Gleeson, R. Q. Grafton, E. Jobbagy, S. Kebede, S.R. Kolusu, L.F. Konikow, D. Long, M. Mekonnen, H.M. Schmied, A. Mukherjee, A. MacDonald, R.C. Reedy, M. Shamsudduha, C.T. Simmons, A. Sun, R.G. Taylor, K.G. Villholth, C. J. Vörösmarty, C. Zheng, Global water resources and the role of groundwater in a resilient water future, Nat. Rev. Earth Environ. 4 (2) (2023) 87–101, https://doi.org/10.1038/s43017-022-00378-6.

[2] T. Si, X. Ma, Z. Liao, H. Chen, B. Liang, S.T. Chu, J. Fan, Highly efficient porous MXene desalination membranes controlled by the thickness of the transition metal carbides, J. Membr. Sci. 715 (2025) 123468, https://doi.org/10.1016/j.memsci.2024.123468.

[3] A.T. Ghonim, H.A. Faiad, M.I. Rashad, S. Ahmed, M.A. Farahat, Assessment of a pilot continuous freezing desalination system with vacuum-assisted brine extraction, Desalination 594 (2025) 118305, https://doi.org/10.1016/j.desal.2024.118305.

[4] X. Liu, X. Xu, X. Xuan, W. Xia, G. Feng, S. Zhang, Z.-G. Wu, B. Zhong, X. Guo, K. Xie, Y. Yamauchi, Unlocking enhanced capacitive deionization of NaTi2(PO4)3/carbon materials by the yolk–shell design, J. Am. Chem. Soc. 145 (16) (2023) 9242–9253, https://doi.org/10.1021/jacs.3c01755.

[5] C. Liu, X. Li, Y. Yao, W. Wu, B. Guo, S. Lu, W. Qin, X. Wu, Reactivation of redox active materials boosts the performance of electrochemical desalination with coupling energy storage, Water Res. 243 (2023) 120396, https://doi.org/10.1016/j.watres.2023.120396.

[6] X. Wu, Y. Lu, X. Ren, P. Wu, D. Chu, X. Yang, H. Xu, Interfacial solar evaporation: from fundamental research to applications, Adv. Mater. 36 (23) (2024) 2313090, https://doi.org/10.1002/adma.202313090.

[7] R. Deng, J. Mo, Y. Yang, Z. Pei, X. Li, Dissecting spacer induced membrane deformation and fluid hydraulic behavior in reverse osmosis, Desalination 595 (2025) 118315, https://doi.org/10.1016/j.desal.2024.118315.

[8] K. Harby, M. Emad, M. Benghanem, T.Z. Abolibda, K. Almohammadi, A. Aljabri, A. Alsaiari, M. Elgendi, Reverse osmosis hybridization with other desalination techniques: an overview and opportunities, Desalination 581 (2024) 117600, https://doi.org/10.1016/j.desal.2024.117600.

[9] Q. Li, L. An, C. Shang, J. Meng, High rejection seawater reverse osmosis TFC membranes with a polyamide-polysulfonamide interpenetrated functional layer, J. Membr. Sci. 715 (2025) 123507, https://doi.org/10.1016/j.memsci.2024.123507.

[10] M. Gao, W. Chen, Engineering strategies toward electrodes stabilization in capacitive deionization, Coord. Chem. Rev. 505 (2024) 215695, https://doi.org/10.1016/j.ccr.2024.215695.

[11] H. Wang, X. Xu, X. Gao, Y. Li, T. Lu, L. Pan, Design of three-dimensional faradic electrode materials for high-performance capacitive deionization, Coord. Chem. Rev. 510 (2024) 215835, https://doi.org/10.1016/j.ccr.2024.215835.

[12] N.H.J. Freire, C.J. Linnartz, L.A. Montoro, V.S.T. Ciminelli, M. Wessling, Flow electrode capacitive deionization with iron-based redox electrolyte, Desalination 578 (2024) 117313, https://doi.org/10.1016/j.desal.2024.117313.

[13] Y. Kim, S. Jeon, D. Ahn, H. Kim, C. Kim, Y. Lee, Parametric investigation of ferri/ferrocyanide redox flow for performance optimization of redox flow desalination, Desalination 550 (2023) 116406, https://doi.org/10.1016/j.desal.2023.116406.

[14] Y. Xiao, H. Chen, M. Li, Q. He, T.Z. Oo, M. Zaw, N.W. Lwin, K.N. Hui, M. Luo, D. Tang, G. Ying, F. Chen, Ionic liquid redox flow desalination of seawater, Desalination 574 (2024) 117284, https://doi.org/10.1016/j.desal.2023.117284.

[15] M. Liang, R. Karthick, Q. Wei, J. Dai, Z. Jiang, X. Chen, T.Z. Oo, S.H. Aung, F. Chen, The progress and prospect of the solar-driven photoelectrochemical desalination, Renew. Sustain. Energy Rev. 155 (2022) 111864, https://doi.org/10.1016/j.rser.2021.111864.

[16] K. Ramalingam, M. Liang, N.L.W. Pyae, S.H. Aung, T.Z. Oo, P. Srimuk, J. Ma, V. Presser, F. Chen, T.D. Waite, Self-sustained visible-light-driven electrochemical redox desalination, ACS Appl. Mater. Interfaces 12 (29) (2020) 32788–32796, https://doi.org/10.1021/acsami.0c08286.

[17] J. Hu, Y. Sun, Z. Liu, B. Zhu, L. Zhang, N. Xu, M. Zhu, J. Zhu, Z. Chen, Photothermal fabrics for solar-driven seawater desalination, Prog. Mater Sci. 150 (2025) 101407, https://doi.org/10.1016/j.pmatsci.2024.101407.

[18] N. Kim, A. Aguda, C. Kim, X. Su, Redox-mediated electrodialysis for desalination, environmental remediation, and resource recovery, ACS Energy Lett. 9 (8) (2024) 3887–3912, https://doi.org/10.1021/acsenergylett.4c00913.

[19] Z. Hu, Y. Chen, Advancements in sustainable desalination with ocean thermal energy: a review, Desalination 586 (2024) 117770, https://doi.org/10.1016/j.desal.2024.117770.

[20] Z. Yang, D. Li, Y. Zhu, X. Zhu, W. Yu, K. Yang, B. Chen, Developing salt-rejecting evaporators for solar desalination: a critical review, Environ. Sci. Tech. 58 (20) (2024) 8610–8630, https://doi.org/10.1021/acs.est.3c09703.

[21] P.J. Choi, J. Lee, A. Jang, Interconnection between renewable energy technologies and water treatment processes, Water Res. 261 (2024) 122037, https://doi.org/10.1016/j.watres.2024.122037.

[22] J. Duan, B. Yu, L. Huang, B. Hu, M. Xu, G. Feng, J. Zhou, Liquid-state thermocells: Opportunities and challenges for low-grade heat harvesting, Joule 5 (4) (2021) 768–779, https://doi.org/10.1016/j.joule.2021.02.009.

[23] Y. Zeng, B. Yu, M. Chen, J. Zhang, P. Liu, J. Guo, J. Wang, G. Feng, J. Zhou, J. Duan, Solvation entropy engineering of thermogalvanic electrolytes for efficient electrochemical refrigeration, Joule 9 (2025) 101822, https://doi.org/10.1016/j.joule.2025.101822.

[24] H.W. Chen, H.Y. Zou, F.H. Zhong, M. Qu, S.Q. Zhao, X. Wei, D.K. Hong, Y.F. Song, Z. Liu, Liquid-flow thermocells with high hybrid entropy for low-grade heat harvesting, Nano Energy 129 (2024) 109992, https://doi.org/10.1016/j.nanoen.2024.109992.

[25] D. Zhang, J. Dai, M. Liang, M. Han, Q. He, F. Chen, L.-J. Li, Thermal redox desalination of seawater driven by temperature difference, ACS Energy Lett. 8 (5) (2023) 2325–2330, https://doi.org/10.1021/acsenergylett.3c00128.

[26] X. He, H. Sun, Z. Li, X. Chen, Z. Wang, Y. Niu, J. Jiang, C. Wang, Redox-induced thermocells for low-grade heat harvesting: mechanism, progress, and their applications, J. Mater. Chem. A 10 (39) (2022) 20730–20755, https://doi.org/10.1039/D2TA05742E.

[27] H. Zhou, H. Inoue, M. Ujita, T. Yamada, Advancement of electrochemical thermoelectric conversion with molecular technology, Angew. Chem. Int. Ed. 62 (2) (2023) 202213449, https://doi.org/10.1002/anie.202213449.

[28] T. Xu, Y. Tao, Y. Qian, W. Li, Z. Ma, Z. Zheng, X. Li, Q. Jiang, Y. Luo, J. Yang, Semi-solid thermo-electrochemical cell based wearable power generator for body heat harvesting, Adv. Funct. Mater. 34 (25) (2024) 2316068, https://doi.org/10.1002/adfm.202316068.

[29] H. Zhang, Z. Wang, H. Li, M. Salla, Y. Song, S. Huang, S. Huang, X. Wang, K. Liu, G. Xu, J. Huang, C.-W. Qiu, Q. Wang, Continuous electricity generation from solar heat and darkness, Joule 7 (7) (2023) 1515–1528, https://doi.org/10.1016/j.joule.2023.06.009.

[30] B. Yu, H. Xiao, Y. Zeng, S. Liu, D. Wu, P. Liu, J. Guo, W. Xie, J. Duan, J. Zhou, Cost-effective n-type thermocells enabled by thermosensitive crystallizations and 3D multi-structured electrodes, Nano Energy 93 (2022) 106795, https://doi.org/10.1016/j.nanoen.2021.106795.

[31] J. Duan, G. Feng, B. Yu, J. Li, M. Chen, P. Yang, J. Feng, K. Liu, J. Zhou, Aqueous thermogalvanic cells with a high Seebeck coefficient for low-grade heat harvest, Nat. Commun. 9 (1) (2018) 5146, https://doi.org/10.1038/s41467-018-07625-9.

[32] B. Yu, J. Duan, H. Cong, W. Xie, R. Liu, X. Zhuang, H. Wang, B. Qi, M. Xu, Z. L. Wang, J. Zhou, Thermosensitive crystallization–boosted liquid thermocells for low-grade heat harvesting, Science 370 (6514) (2020) 342–346, https://doi.org/10.1126/science.abd6749.

[33] M. Khatibi, S.N. Ashrafizadeh, Ion transport in intelligent nanochannels: a comparative analysis of the role of electric field, Anal. Chem. 95 (49) (2023) 18188–18198, https://doi.org/10.1021/acs.analchem.3c03809.

[34] M. Khatibi, S.N. Ashrafizadeh, Mitigating Joule heating in smart nanochannels: Evaluating the efficacy of AC vs. DC fields, Int. Commun. Heat Mass Transfer 154 (2024) 107448, https://doi.org/10.1016/j.icheatmasstransfer.2024.107448.

[35] A. Heydari, M. Khatibi, S.N. Ashrafizadeh, Manipulation of ionic transport behavior in smart nanochannels by diffuse bipolar soft layer, Phys. Fluids 36 (11) (2024) 112026, https://doi.org/10.1063/5.0232567.

[36] A. Aminnia, M. Khatibi, S. Nezameddin Ashrafizadeh, Fouling minimization with nanofluidic membranes; How electric field may help, Sep. Purif. Technol. 325 (2023) 124698, https://doi.org/10.1016/j.seppur.2023.124698.

[37] W. Shan, Y. Zi, H. Chen, M. Li, M. Luo, T.Z. Oo, N.W. Lwin, S.H. Aung, D. Tang, G. Ying, F. Chen, Y. Chen, Coupling redox flow desalination with lithium recovery from spent lithium-ion batteries, Water Res. 252 (2024) 121205, https://doi.org/10.1016/j.watres.2024.121205.

[38] J. Wu, Y. Gong, K. Du, G. Hu, K. Bai, Z. Peng, X. Chen, F. Liu, Y. Cao, Selective oxidative leaching and restoration of FePO4 from spent LiFePO4 powder for regeneration into LiFePO4 cathode, Sep. Purif. Technol. 359 (2025) 130674, https://doi.org/10.1016/j.seppur.2024.130674.

[39] D. Zhou, X. Qiu, F. Liang, S. Cao, Y. Yao, X. Huang, W. Ma, B. Yang, Y. Dai, Comparison of the effects of FePO4 and FePO4·2H2O as precursors on the electrochemical performances of LiFePO4/C, Ceram. Int. 43 (16) (2017) 13254–13263, https://doi.org/10.1016/j.ceramint.2017.07.023.

[40] H. Zhang, F. Zhang, J. Yu, M. Zhou, W. Luo, Y.M. Lee, M. Si, Q. Wang, Redox targeting-based thermally regenerative electrochemical cycle flow cell for enhanced low-grade heat harnessing, Adv. Mater. 33 (5) (2021) 2006234, https://doi.org/10.1002/adma.202006234.

[41] Y. Chen, M. Zhou, Y. Xia, X. Wang, Y. Liu, Y. Yao, H. Zhang, Y. Li, S. Lu, W. Qin, X. Wu, Q. Wang, A stable and high-capacity redox targeting-based electrolyte for aqueous flow batteries, Joule 3 (9) (2019) 2255–2267, https://doi.org/10.1016/j.joule.2019.06.007.

[42] J. Yu, L. Fan, R. Yan, M. Zhou, Q. Wang, Redox targeting-based aqueous redox flow lithium battery, ACS Energy Lett. 3 (10) (2018) 2314–2320, https://doi.org/10.1021/acsenergylett.8b01420.

[43] W. Wang, Y. Gang, Z. Hu, Z. Yan, W. Li, Y. Li, Q.-F. Gu, Z. Wang, S.-L. Chou, H.-K. Liu, S.-X. Dou, Reversible structural evolution of sodium-rich rhombohedral Prussian blue for sodium-ion batteries, Nat. Commun. 11 (1) (2020) 980, https://doi.org/10.1038/s41467-020-14444-4.

[44] T. Kim, J.S. Lee, G. Lee, H. Yoon, J. Yoon, T.J. Kang, Y.H. Kim, High thermopower of ferri/ferrocyanide redox couple in organic-water solutions, Nano Energy 31 (2017) 160–167, https://doi.org/10.1016/j.nanoen.2016.11.014.

[45] J. Wu, J.J. Black, L. Aldous, Thermoelectrochemistry using conventional and novel gelled electrolytes in heat-to-current thermocells, Electrochim. Acta 225 (2017) 482–492, https://doi.org/10.1016/j.electacta.2016.12.152.

[46] P. Yang, K. Liu, Q. Chen, X. Mo, Y. Zhou, S. Li, G. Feng, J. Zhou, Wearable thermocells based on gel electrolytes for the utilization of body heat, Angew. Chem. Int. Ed. 55 (39) (2016) 12050–12053, https://doi.org/10.1002/anie.201606314.

[47] L. Jin, G.W. Greene, D.R. MacFarlane, J.M. Pringle, Redox-active quasi-solid-state electrolytes for thermal energy harvesting, ACS Energy Lett. 1 (4) (2016) 654–658, https://doi.org/10.1021/acsenergylett.6b00305.

[48] Y. Liu, S. Zhang, Y. Zhou, M.A. Buckingham, L. Aldous, P.C. Sherrell, G.G. Wallace, G. Ryder, S. Faisal, D.L. Officer, S. Beirne, J. Chen, Advanced wearable thermocells for body heat harvesting, Adv. Energy Mater. 10 (48) (2020) 2002539, https://doi.org/10.1002/aenm.202002539.

[49] R. Hu, B.A. Cola, N. Haram, J.N. Barisci, S. Lee, S. Stoughton, G. Wallace, C. Too, M. Thomas, A. Gestos, M.E.d. Cruz, J.P. Ferraris, A.A. Zakhidov, R.H. Baughman, Harvesting waste thermal energy using a carbon-nanotube-based thermo-electrochemical cell, Nano Lett. 10(3) (2010) 838-846. doi: 10.1021/nl903267n.

[50] M.S. Romano, N. Li, D. Antiohos, J.M. Razal, A. Nattestad, S. Beirne, S. Fang, Y. Chen, R. Jalili, G.G. Wallace, R. Baughman, J. Chen, Carbon nanotube – reduced graphene oxide composites for thermal energy harvesting applications, Adv. Mater. 25 (45) (2013) 6602–6606, https://doi.org/10.1002/adma.201303295.

[51] K. Kim, S. Hwang, H. Lee, Unravelling ionic speciation and hydration structure of Fe(III/II) redox couples for thermoelectrochemical cells, Electrochim. Acta 335 (2020) 135651, https://doi.org/10.1016/j.electacta.2020.135651.

[52] A. Kundu, T.S. Fisher, Harnessing the thermogalvanic effect of the ferro/ferricyanide redox couple in a thermally chargeable supercapacitor, Electrochim. Acta 281 (2018) 357–369, https://doi.org/10.1016/j.electacta.2018.05.164.

[53] H. Im, T. Kim, H. Song, J. Choi, J.S. Park, R. Ovalle-Robles, H.D. Yang, K.D. Kihm, R.H. Baughman, H.H. Lee, T.J. Kang, Y.H. Kim, High-efficiency electrochemical thermal energy harvester using carbon nanotube aerogel sheet electrodes, Nat. Commun. 7 (1) (2016) 10600, https://doi.org/10.1038/ncomms10600.

[54] S.-M. Jung, J. Kwon, J. Lee, B.-J. Lee, K.-S. Kim, D.-S. Yu, Y.-T. Kim, Hybrid thermo-electrochemical energy harvesters for conversion of low-grade thermal energy into electricity via tungsten electrodes, Appl. Energy 299 (2021) 117334, https://doi.org/10.1016/j.apenergy.2021.117334.

[55] S. Wei, J. Ma, D. Wu, B. Chen, C. Du, L. Liang, Y. Huang, Z. Li, F. Rao, G. Chen, Z. Liu, Constructing flexible film electrode with porous layered structure by MXene/SWCNTs/PANI ternary composite for efficient low-grade thermal energy harvest, Adv. Funct. Mater. 33 (13) (2023) 2209806, https://doi.org/10.1002/adfm.202209806.

[56] X. He, H. Sun, Z. Li, J. Song, H. Li, C. Wang, Y. Niu, J. Jiang, Simultaneously enhanced energy harvesting and storage performance achieved by 3D mix-phase Mose2-Nise/NF, Adv. Funct. Mater. 34 (7) (2024) 2307835, https://doi.org/10.1002/adfm.202307835.

[57] H. Dartoomi, M. Khatibi, S.N. Ashrafizadeh, Enhanced ionic current rectification through innovative integration of polyelectrolyte bilayers and charged-wall smart nanochannels, Anal. Chem. 95 (2) (2023) 1522–1531, https://doi.org/10.1021/acs.analchem.2c04559.

[58] A. Alinezhad, M. Khatibi, S.N. Ashrafizadeh, Ionic transfer behavior of bipolar nanochannels resembling PNP nanotransistor, Electrochim. Acta 460 (2023) 142625, https://doi.org/10.1016/j.electacta.2023.142625.

[59] S. Jafari, M. Khatibi, S.N. Ashrafizadeh, Blue energy conversion utilizing smart ionic nanotransistors, Electrochim. Acta 507 (2024) 145186, https://doi.org/10.1016/j.electacta.2024.145186.

[60] M. Khatibi, S.K. Mehta, S.N. Ashrafizadeh, P.K. Mondal, Surface charge-dependent slip length modulates electroosmotic mixing in a wavy micromixer, Phys. Fluids 36 (7) (2024) 073105, https://doi.org/10.1063/5.0218566.